International Journal of Innovative Technology and Exploring Engineering (IJITEE)
ISSN: 2278-3075 (Online), Volume-9 Issue-6, April 2020

Enhancement in DC Electrical Resistivity and Dielectric Behaviour of Ti^{4+} Doped $CoFe_2O_4$ NP's for Nanoelectronics Application

B. A. Patil, Jitendra S. Kounsalye, K. M. Jadhav, R. D. Kokate

Abstract: ***Inverse spinel structured cobalt ferrite is one of the capable nominee for information storage and also in nanoelectronics devices. The present paper reports the rietveld refined structural, elastic, electrical and dielectric behaviour of titanium doped $CoFe_2O_4$ NP's. The synthesis of $Co_{1+x}Ti_xFe_{2-2x}O_4$ (where, $0.0 \leq x \leq 0.5$) nanoparticles was performed using self generated combustion technique. The prepared NP's were characterized by X-ray diffraction technique (XRD) and Fourier transform infrared spectroscopy (FT-IR) technique to analyze the structural and elastic properties. The analysis of XRD patterns confirms the formation of single phase spinel cubic structure of all the prepared samples. The diffractograms obtained at room temperature were used for Rietveld refinement to determine the lattice constant, oxygen position, average crystallite size etc. parameters. The elastic modules were investigated through vibrational bands in FTIR spectra. The band positions in FT-IR spectra confirmed the octahedral [B] and tetrahedral (A) stretching which evident the ferrite skeleton. The plot of DC electrical resitivity with respect to temperature shows the semiconducting behaviour of the nanoparticles. The activation energy determined through resistivity plots, show decreasing nature with incrementing Ti^{4+} doping in cobalt ferrite. The dielectric parameters decreased exponentially with increasing frequency and with Ti doping.***

Keywords: ***Co-Ti Ferrite, Rietveld Refinement, Elastic properties; DC Resistivity and Dielectric properties.***

I. INTRODUCTION

Spinel ferrite represented by the formula MFe_2O_4 have been explored for various technological applications from last some decades [1-3]. The unique characteristics of these materials are that, they exhibit both electrical as well as magnetic properties.

Revised Manuscript Received on April 30, 2020.
***** Correspondence Author
K. M. Jadhav*, Department of Physics, Dr. Babasaheb Ambedkar Marathwada University, Aurangabad, (MS) India. E-mail: drjadhavkm@gmail.com
B. A. Patil, Department of Physics, Dr. Babasaheb Ambedkar Marathwada University, Aurangabad, (MS) India.
Jitendra S. Kounsalye, Department of Physics, Dr. Babasaheb Ambedkar Marathwada University, Aurangabad, (MS) India.
R. D. Kokate, Department of Physics, Dr. Babasaheb Ambedkar Marathwada University, Aurangabad, (MS) India.

They are non-replaceable candidates in memory storage device, transformer core, energy storage device, gas sensing, microwave devices, etc [4-10] on account of their excellent magnetic and electrical properties [11-13].

Recently, with the development of nanoscience and nanotechnology magnetic nanoparticles of spinel ferrite have attracted attention of many researchers [14]. The chemical stability, nanosize dimension, large surface to volume ratio, greater homogeneity, easy preparation etc are the remarkable features of magnetic nanoparticles [15]. Owing to these properties, spinel ferrite nanoparticles currently have been used in various fields such as sensors, catalyst, water purification, targeted drug delivery, hyperthermia etc [16-21]. The properties of the spinel ferrite nanoparticles are sensitive to various factors like synthesis procedure, synthesis parameters, chemical composition, nature and type of dopant. Usually, spinel ferrite nanoparticles were prepared by wet chemical methods which include chemical coprecipitation, hydrothermal, freeze drying, sol-gel auto combustion, microemulsions etc. Among these methods, sol-gel auto combustion technique has many advantages such as it gives homogeneous particle distribution, it does not require large temperature, special environment, and expensive setup [22, 23]. Spinel ferrites are structurally analogues with the mineral $MgAl_2O_4$ and have the general formula $(M)^{II}\ [Fe_2]^{III}\ O_4^{2-}$. Here, M represents divalent metal ion like Co, Ni, Zn, Cu, Cd etc. It crystallizes in a FCC structure corresponding to the Fd3m space group and possesses 8 molecular formula units. The unit cell of spinel ferrite possesses tetrahedral (A) and octahedral [B] sites in which cations of different size and valence can accommodate. Cobalt ferrite is a unique candidate amongst the all spinel ferrite. It possesses inverse spinel structure in which Co^{2+} ions mostly occupy octahedral [B] site. Cobalt ferrite show high electrical resistivity, high saturation magnetization, high Curie temperature, high magnetocrystalline anisotropy constant etc. Owing to these important electrical and magnetic properties cobalt ferrites have applications in many areas including high frequency devices, sensors, gyrators, circulators etc [24-26].

In the literature, large numbers of reports are available on synthesis and characterizations of cobalt ferrite nanoparticles. The properties of $CoFe_2O_4$ NP's are chiefly administered by doping two/three/four valence ions. $CoFe_2O_4$ with doping of Zn^{2+}, Al^{3+}, Sn^{4+} etc. were explored by number of researchers. ***P. T. Phong et al.*** studied the influence of Zn^{2+} content on the magneto-optical properties of $CoFe_2O_4$ NP's prepared by hydrothermal method at low temperature [27].

A. Sathiya Priya et al. studied the effect of Al^{3+} substitution on the structural, electric and impedance behavior of cobalt ferrite nanoparticles [28]. ***K Ugendar et al.*** reported the temperature-dependent magnetization, anisotropy and conductivity of Sn^{4+} substituted cobalt ferrite nanoparticles [29]. Titanium is a non magnetic tetravalent ion can occupy octahedral [B] site.

The replacement of Fe^{3+} ions at octahedral [B] site by Ti^{4+} ions can lead to interesting electrical and dielectric properties which may be useful for microwave applications.

In the present communication, we report the synthesis, Rietveld refined structural properties, infrared, elastic, DC electrical resistivity and dielectric behaviour of Ti doped $CoFe_2O_4$ NP's.

II. EXPERIMENTAL TECHNIQUES

A. Synthesis

Tetravalent Ti^{4+} substituted $CoFe_2O_4$ NP's with general chemical recipe '$o_{1+x}Ti_xFe_{2-2x}O_4$' ($0.0 \le x \le 0.50$, with 0.10 step rate) were prepared using self generated combustion method. The raw materials used for the synthesis are $C_{16}H_{36}O_4Ti$, nitrates of cobalt and iron and $C_6H_8O_7$. All the chemicals used were of AR grade. By implementing the propellant chemistry oxidants to fuel ratio was picked as 1:3. The corresponding nitrates and citric acid were dissolved separately in 100ml distilled water and $C_{16}H_{36}O_4Ti$ in C_2H_6O. Finally, all the solutions mixed together and the mixture called sol is adjusted to neutral (pH 7) by using ammonia. The neutral sol was heated continually at 90˚C up to the formation of gel and then suddenly combustion takes place by forming porous ash [30, 31]. The ash was grind and the obtained fine powder was annealed at 650˚C for 6h to remove any impurity remained.

B. Characterization Tools

All the samples were analyzed by Regaku X-ray diffraction meter (XRD). The XRD peaks were collected in the 2θ scope of 20-80˚ by Cu-K_α rays. The characteristics peaks are determined by Vortex 80 Fourier transform infrared FT-IR tool. The FTIR spectra were determined in the wavenumber scope of 400-4000 cm^{-1}. The magnetic properties of samples were carried out using pulse field hysteresis loop tracer technique at room temperature by applying ± 5kOe field.

III. RESULTS AND DISCUSSION

A. X-ray diffraction analysis

The single phase formation of all the samples of $Co_{1+x}Ti_xFe_{2-2x}O_4$ ($0.0 \le x \le 0.50$, in step of 0.10) was identified at room temperature using X-ray diffractometer (Ultima IV of Rigaku Corporation, Japan) with Cu-K_α radiation having wavelength of 1.54 Å. The analysis of XRD patterns of all the samples confirms the formation of single phase cubic spinel structure. The diffraction patterns matches well with JCPDS card number #*221086*. The Rietveld method is a well known technique to obtain various structural details such as lattice parameter, profile shape, width etc parameters from powder diffraction data. The Rietveld method comprises a least square procedure to compare Bragg's peak intensities and those calculated from possible structural details. All the samples were analyzed using Rietveld refinement. The fitting superiority of the investigational data is evaluated by calculating the goodness of fit χ^2 and R factor. When these parameters approaches to their lower value the best fit to the experimental diffraction data is achieved. Rietveld refined XRD patterns of $Co_{1+x}Ti_xFe_{2-2x}O_4$ NP's was shown in fig. 1.

The refinement results show that all the patterns exhibit monophase cubic spinel structure. No other impurity peaks was detected in any XRD patterns. The intense, sharp and broad peaks indicate the nanocrystalline behaviour of all the samples. The R factor such as profile factor (R_p), weighted profile factor (R_{wp}), expected R-factor (R_{exp}) and goodness factor (χ^2) obtained from Rietveld analysis are tabulated in table 1 [32, 33].

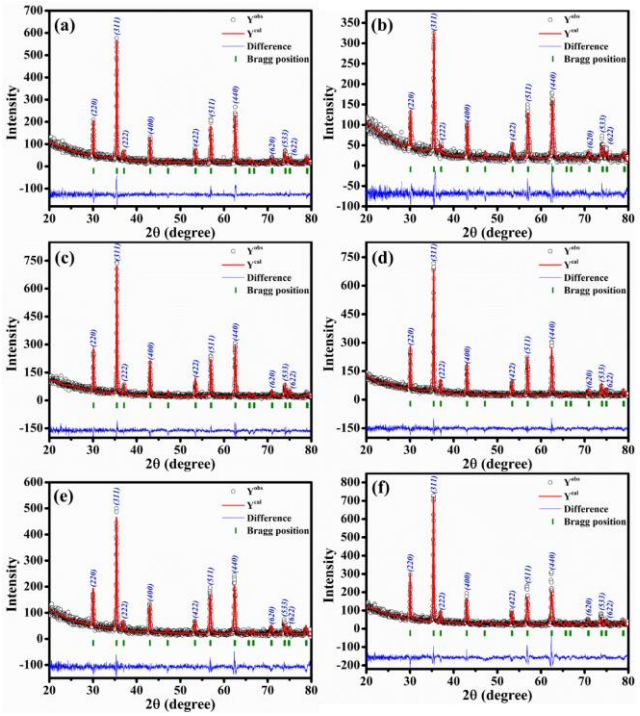

Fig. 1 Rietveld refined XRD patterns for $Co_{1+x}Ti_xFe_{2-2x}O_4$ samples

The analysis of the crystallite size has been carried out by using the broadening of the XRD patterns. The crystallite size was determined by using Scherrer's relation,

$D = k \lambda / \beta \cos\theta$,

where, the constant k is 0.89, β is the FWHM of the most intense peak (311) and λ the wavelength of the Cu-K_α radiation, θ is the Bragg's diffraction angle and D is the crystallite size. The values of crystallite size are provided in table 1.

The allocation of the cations over the accessible tetra (A) and octa [B] sites has been obtained from site occupancy factor. The site possession of the cations (Co^{2+}, Fe^{3+} & Ti^{4+}) in the available two sites i.e. (A) and [B] are constrained so as to preserve the stoichiometric composition of the martial. It is assumed that, sum of cationic distribution for tetra A site is one & two for octa B site. In determining the cation distribution it was assumed that,

cobalt ferrite possesses inverse spinel structure, cobalt (Co^{2+}) and titanium (Ti^{4+}) both occupies octahedral B site according to the literature reports. The proposed cation distribution of the present samples is presented in table 2.

Table- I: 'Rietveld parameters; R_p, R_{wp}, R_{exp} and χ^2 for $Co_{1+x}Ti_xFe_{2-2x}O_4$ nanoparticles'

x	R_P	R_{WP}	R_{exp}	χ^2
0.00	66.7	43.1	43.1	1.00
0.10	71.6	50.3	46.9	1.15
0.20	55.1	44.5	38.4	1.34
0.30	55.8	40.8	40.8	1.00
0.40	60.8	46.1	42.3	1.19
0.50	48.2	40.4	30.8	1.73

Table- II: Cation distribution inferred from site occupancy factor (Rietveld) and oxygen positional parameter (u) Co1+xTixFe2-2xO4 nanoparticles

x	*Deduced formula of the product*	*Cation distribution*	*u (Å)*
0.00	$CoFe_2O_4$	$(Fe_1)[Co_1Fe_1]O_4$	0.3783
0.10	$Co_{1.1}Ti_{0.1}Fe_{1.8}O_4$	$(Fe_1)[Co_{1.1}Ti_{0.1}Fe_{0.8}]O_4$	0.3782
0.20	$Co_{1.2}Ti_{0.2}Fe_{1.6}O_4$	$(Fe_1)[Co_{1.2}Ti_{0.2}Fe_{0.6}]O_4$	0.3781
0.30	$Co_{1.3}Ti_{0.3}Fe_{1.4}O_4$	$(Fe_1)[Co_{1.3}Ti_{0.3}Fe_{0.4}]O_4$	0.3780
0.40	$Co_{1.4}Ti_{0.4}Fe_{1.2}O_4$	$(Fe_1)[Co_{1.4}Ti_{0.4}Fe_{0.2}]O_4$	0.3779
0.50	$Co_{1.5}Ti_{0.5}Fe_{1.0}O_4$	$(Fe_1)[Co_{1.5}Ti_{0.5}]O_4$	0.3777

The refined XRD data was used to compute the lattice parameter by following equation,

$$\frac{\lambda^2}{a_{ex}^2} = \frac{sin^2\theta}{(h^2+k^2+l^2)} \quad \ldots\ldots (1)$$

The lattice constant increased with increment in Ti^{4+} replacement. The increment in lattice constant is attributed to the dissimilarity in ionic radii of the constituent ions. The ionic radii of Fe^{3+}, Co^{2+} and Ti^{4+} are 0.67Å, 0.72 Å, 0.54 Å respectively. In the current scenario two Fe^{3+} ions are substituted by grouping of divalent Co^{2+} and tetravalent Ti^{4+}. Therefore, the lattice constant of the present samples get increased after Ti^{4+} doping. Furthermore, with substitution of Ti^{4+}, the (311) reflex is reallocated towards low angle as appeared in the fig. 2 which suggests the lattice parameter increase with Ti substitution. The theoretical lattice constant (a_{th}) was determined by the equation,

$a_{th} = 8/3 * 3^{1/2} * [(r_A+R_0) + 3^{1/2} (r_B+R_0)]$

The crystallite sizes were calculated by both the Scherrer's method and Williamson-Hall (W-H) method. The values of the crystallite sizes are provided in table 3. The crystallite size values determined from W-H method are fairly agreed with the values calculated from Scherrer's relation. The values of r_A and r_B were computed using the cation distribution given in table 2. Table 2 also shows the values of theoretical lattice constant (a_{th}) and the lattice constant obtained through Rietveld analysis.

Table- III: Tetra and octa ionic radii (rA and rB), Lattice parameters theoretical (ath), experimental (aex) and inferred from Rietveld refinement (art)

x	a_{ex} (Å)	r_A (Å)	r_B (Å)	a_{th} (Å)	a_{rt} (Å)	D (nm)	
						Scherrer	*W-H*
0.00	8.365	0.490	0.695	8.412	8.395	37	42
0.10	8.366	0.490	0.698	8.420	8.397	34	31
0.20	8.370	0.490	0.701	8.428	8.400	40	47
0.30	8.382	0.490	0.704	8.436	8.406	42	52
0.40	8.385	0.490	0.707	8.444	8.412	36	34
0.50	8.386	0.490	0.710	8.452	8.414	41	77

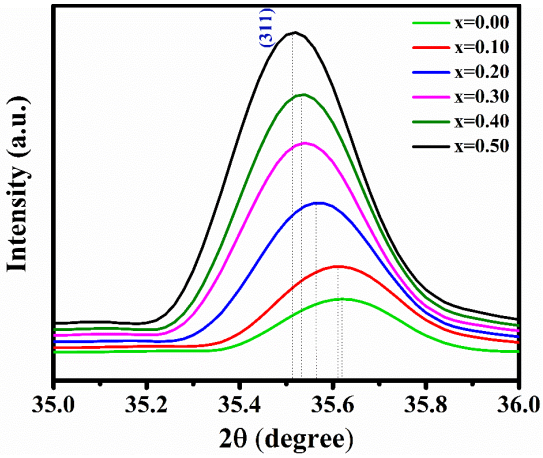

Fig. 2 The shift of most intense peak (311) for Co1+xTixFe2-2xO4 samples

Table- IV: X-ray density (dx), bulk density (dB), porosity (P) and volume of unit cell (V) for Co1+xTixFe2-2xO4 nanoparticles

x	d_x	d_B	P	V
	(gm/cm^3)		*%*	*(Å^3)*
0.00	5.324	4.491	15.547	585.398
0.10	5.313	4.485	15.596	585.530
0.20	5.296	4.466	15.686	586.352
0.30	5.263	4.415	16.110	588.961
0.40	5.249	4.391	16.356	589.460
0.50	5.237	4.366	16.631	589.735

Equation 2 was used to estimate oxygen positional parameter (u) [34] and the values are proovided in Table 2.

$$u = \frac{(r_A+R_O)}{a_{th}\sqrt{3}} + \frac{1}{4} \quad \ldots\ldots (2)$$

From the cationic allocation it is clear that the expansion of octahedral site due to substitution was occur and hence dislocation of anions takes place. This results in decrease in the values of u was observed [35].

The X-ray density was calculated from theoretical lattice parameter (a_{th}) using equation (3) [36],

$$\rho = \frac{8M}{N_A V} \quad \ldots\ldots (3)$$

X-ray density was found to decrease with the replacement of Ti ions, which might be due to increment in volume of the unit cell. Archimedes principle was used to determine the bulk density and porosity of present investigated samples and listed in Table 3. The bulk density of the cobalt ferrite gets decreased and porosity was increases after substitution.

B. Fourier Transform Infrared Spectroscopy (FTIR)

Ferrites are constantly bonded crystal and the atoms are bonded to all nearest neighbors [37]. The geometrical arrangement of spinel ferrites are composed of two dissimilar sublattices namely tetra (A) and octa [B]. The tetrahedral ions oscillates through the direction of bonding of cations and neighboring oxygen ions, whereas the octahedral ions oscillates perpendicular to it [38]. The stretching of these two sublattices leads to find two absorption bands in FTIR spectra, the band at ~600 cm^{-1} corresponds to the tetra site and other one at ~400 cm^{-1} to the octa site. In the present study,

FTIR spectra of the present samples is presented in Fig. 2. The corresponding band positions are tabulated in Table 5. Two primary bands ν_1 and ν_2 was observed in the spectra and both shifted to a lower frequency with the substitution. The difference in the distance of cations and anions lead to change in the vibrational modes. It is reported that, Fe-O distance at tetrahedral lattice is small than octahedral site (1.99 Å) [39].

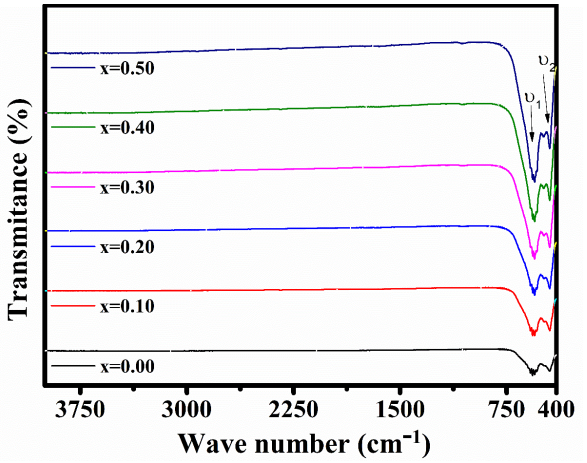

Fig. 3 The FTIR spectra of Co1+xTixFe2-2xO4 samples

The force constant per atom corresponding to the tetrahedral (k_t) and octa (ko) site were determined using relation given by Waldron [37]. The molecular weights of corresponding sites are estimated by the site occupancy given in Table 5 which was used to calculate the k_t and k_o. The Debye temperature θ_D was calculated using the relation given by Waldron [37] & the obtained values are listed in Table 5. It is notified from table 5 that, k_t, k_o, K and θ_D decreases with increase in Ti^{4+} substitution x.

The elastic behaviour of nanoferrites may be obtained from infrared spectroscopy data. The method was proposed by Modi et al. and is useful for our present samples [40]. According to Waldron wave velocity (longitudinal and transverse) can be given by,

$V_l = (C_{11}/\rho)^{1/2}$

$V_t = V_l / 3^{1/2}$

The mean elastic wave velocity (V_L), rigidity modulus (G) and Poisson's ratio (P) of the present system were calculated (Table 6) using the values of V_l and V_t.

Bulk modulus (B)

The bulk modulus (B) is given by $B = 1/3 [C_{11} + 2 C_{12}]$. As per the Waldron, for spinel ferrite $C_{11} = C_{12}$. Therefore, Bulk modulus is equal to the C_{11} or C_{12}. The force constant K is nothing but the product of lattice constant and stiffness constant. The values of bulk modulus (B) obtained in this way are given in table 5. It can be noted that bulk modulus decreases slightly with Ti substation.

Rigidity modulus (G)

The rigidity modulus (G) was calculated using the relation $G = \rho V_t^2$ where ρ is the density and V_t is the transverse elastic wave velocity. The values of rigidity modulus are listed in table 6. It is seen from this table that, like bulk modulus, rigidity modulus also decreases with Ti substitution.

Poisson ratio (σ)

The Poisson ratio (σ) was calculated according to the relation $\sigma = (3B - 2G) / (6B + 2G)$ Table 6 shows the values of Poisson ratio which decreases with Ti substitution.

Young's modulus (E)

The Young's modulus (E) was calculated by the relation $E = (1 + \sigma) + 2 G$. The values of Young's modulus listed in table show decreasing trend with increase in Ti substitution.

Mean elastic wave velocity (Vm)

The mean elastic wave velocity (V_m) was calculated according to the relation,

$Vm = [(V_s^3 + V_l^3) / (V_s^3 + 2 V_l^3)]^{1/3}$

The values of mean elastic wave velocity are given in table 6. The intensification binding energy among a variety of atoms of sublattices leads to change in the elastic moduli [41]. The weakening of interatomic bonding after substitution leads to decrease in elastic moduli. Comparable outcomes were noted in literature for other ferrite systems [42].

Table- V: Infrared bands, M.W. of sublattices (MA, MB), force constant (kt, ko, k) and Debye temperature for Co1+xTixFe2-2xO4 nanoparticles

x	υ_1	υ_2	M_A	M_B	k_t	k_o	K	θ_D (K)
	(cm^{-1})		(kg/mol)		$10^2 \times$ (N/m)			
0.00	568	447	0.06	0.16	1.47	1.73	1.60	731
0.10	556	447	0.06	0.16	1.41	1.67	1.54	719
0.20	553	447	0.06	0.15	1.39	1.62	1.51	720
0.30	552	447	0.06	0.15	1.39	1.56	1.48	719
0.40	550	447	0.06	0.14	1.38	1.50	1.44	725
0.50	548	447	0.06	0.14	1.37	1.45	1.41	733

Table 6: Elastic parameters for Co1+xTixFe2-2xO4 nanoparticles

x	V_L	V_t	B	G	P	V_m
	(m/s)			GPa		(m/s)
0.00	5903	3408	185.52	61.84	0.68	4410
0.10	5779	3337	177.46	59.15	0.65	4317
0.20	5744	3316	174.71	58.24	0.64	4291
0.30	5695	3288	170.70	56.90	0.63	4254
0.40	5681	3280	169.41	56.47	0.62	4244
0.50	5686	3283	169.30	56.43	0.62	4247

C. DC Electrical Resistivity

The DC electrical resistivity and activation energy were studied using two probe technique as a function of temperature. Fig. 3 represents DC resistivity plots. The plot exhibits a typical nature which is similar to the Arrhenius plot. It is evident from Fig. 3 that DC electrical resistivity decreases with temperature increment obeying the relation $\rho = \rho_0 \exp(\Delta E/kT)$. According to Verwey's model, the conduction in the ferrites occurred via the hopping of e^- among Fe^{2+} and Fe^{3+} at octa [B] site. Hopping means substitution of charge between the same elements. In nanocrystalline spinel ferrite the concentration of Fe^{2+} and Fe^{3+} at octa [B] site has a strong influence on the DC electrical resistivity.

Hopping of electrons may also possible between octa [B] and tetra (A) site. The lower temperature province corresponds to ferromagnetic region, while high temperature region corresponds to the paramagnetic region. The conduction mechanism is found to be different in these two regions i.e. ferromagnetic and paramagnetic region. In ferromagnetic region the hopping of negative charge carriers between ferrous (Fe^{2+}) and ferric (Fe^{3+}) ions has been observed while in paramagnetic region polaron hopping is dominant. As a result, the specific resistance of spinel ferrite is decreased with the increase of temperature.

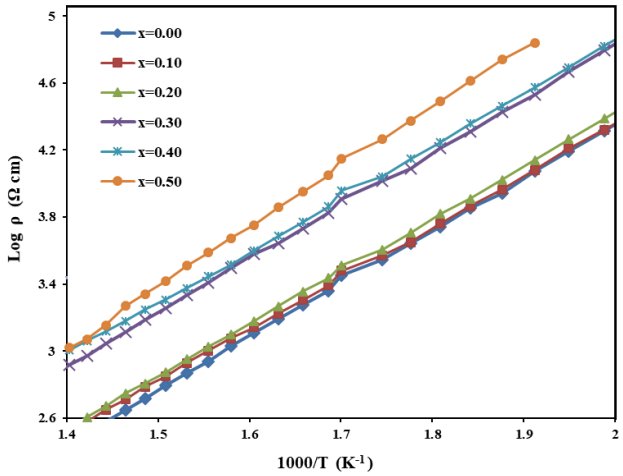

Fig. 4 Arrhenius plots of Co1+xTixFe2-2xO4 system

D. Dielectric properties

In the present study, the frequency dependence of the dielectric properties like dielectric constant (ε′) and dielectric loss (ε′′) and dielectric loss tangent (tanδ) were investigated at room temperature as a function of frequency (20 Hz to 5 MHz) using LCR-Q meter. The dielectric constant (ε′) for all the samples was calculated using the following standard formula:

$$\varepsilon' = \frac{Cd}{\varepsilon_{\circ} A} \quad \ldots 1$$

Fig. 4 represents the variation of frequency-dependent dielectric constant (ε) of all the samples recorded. It can be noted from figure 4 that all the samples exhibit dielectric dispersion. The dielectric constant (ε) reduces with increase in frequency in exponential manner.

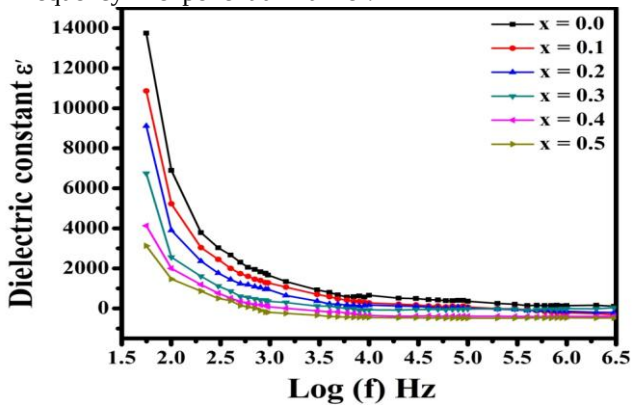

Fig. 5 Variation of dielectric constant with log of frequency for Co1+xTixFe2-2xO4 system

At high frequency, the dielectric dispersion remains almost independent of applied external field. Similar behaviour of dielectric constant as a function of frequency was reported in literature. The decrease in dielectric constant might be clarified by assuming that mechanism of polarization process in ferrite is similar to that of conduction process. It is reported that effect of polarization is to reduce the field. The electronic exchange between ferrous (Fe^{2+}) and ferric (Fe^{3+}) ions cannot follow the alternating field. Hence dielectric constant may decrease substantially as frequency is increased.

The dielectric loss tangent can be calculated by the relation $\tan\delta = \varepsilon''/\varepsilon'$, where δ is the loss angle, ε′ is the real part of dielectric constant and ε″ is the imaginary part. Fig. 7 depicts the variation of ε″ as a function of frequency at room temperature.

It is noted in Fig. 7, that variation of dielectric loss tangent shows the similar dispersion as that of dielectric constant. The dielectric loss tangent decreases exponentially with increase in frequency. At low frequency, dielectric loss tangent decreases suddenly while at high frequency dielectric loss tangent decreases very slowly.

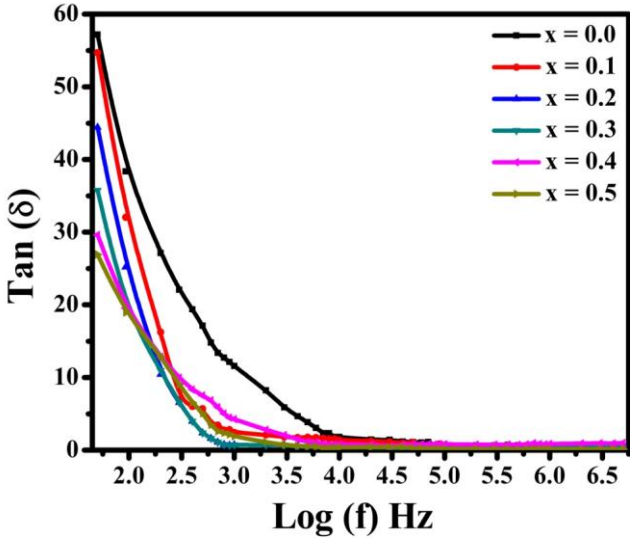

Fig. 6 Variation of dielectric loss tangent with log of frequency for Co1+xTixFe2-2xO4 system

IV. CONCLUSION

The nanocrystalline Ti^{4+} doped $CoFe_2O_4$ NP's was productively prepared by a self generated combustion way. The Rietveld refinement patterns of XRD patterns show the configuration of mono phase spinel cubic formation. The average grain size values determined from SEM images is in the nanometer regime. The stretching vibrations along octahedral and tetrahedral site were confirmed from FTIR spectra. The elastic properties were decremented after the incorporation of Ti^{4+} ions in cobalt ferrite. The DC electrical resitivity displayed the semi conductive behavior of the nanoparticles. The dielectric parameters decreased exponentially with increase in frequency and with Ti doping. The obtained properties of Ti doped $CoFe_2O_4$ are useful for nanoelectronics application.

ACKNOWLEDGMENT

One of the authors B. A. Patil is thankful to Solapur University, Solapur for providing X-ray diffraction facility, Dr. S. M. Patange, Shrikrishna Mahavidyalay, Gunjoti for providing dielectric measurements.

REFERENCES

1. F. da Silva, Journal of nanoscience and nanotechnology, 19 (2019) 4888-4902.
2. P.B. Kharat, S.B. Somvanshi, J.S. Kounsalye, S.S. Deshmukh, P.P. Khirade, K. Jadhav, Temperature dependent viscosity of cobalt ferrite/ethylene glycol ferrofluids, in: AIP Conference Proceedings, AIP Publishing, 2018, pp. 050044.
3. P.B. Kharat, S. More, S.B. Somvanshi, K. Jadhav, Exploration of thermoacoustics behavior of water based nickel ferrite nanofluids by ultrasonic velocity method, Journal of Materials Science: Materials in Electronics, 30 (2019) 6564-6574.
4. M. Amiri, Advances in colloid and interface science, (2019).
5. M. Amiri, Advances in colloid and interface science, (2019).
6. C.-Y. Tsay, Physica B: Condensed Matter, (2019).
7. S.B. Somvanshi, R.V. Kumar, J.S. Kounsalye, T.S. Saraf, K. Jadhav, Investigations of structural, magnetic and induction heating properties of surface functionalized zinc ferrite nanoparticles for hyperthermia applications, in: AIP Conference Proceedings, AIP Publishing, 2019, pp. 030522.
8. V. Bharati, S.B. Somvanshi, A.V. Humbe, V. Murumkar, V. Sondur, K. Jadhav, Influence of trivalent Al–Cr co-substitution on the structural, morphological and Mössbauer properties of nickel ferrite nanoparticles, Journal of Alloys and Compounds, 821 (2020) 153501.
9. S.R. Patade, D.D. Andhare, S.B. Somvanshi, P.B. Kharat, S. More, K. Jadhav, Preparation and Characterizations of Magnetic Nanofluid of Zinc Ferrite for Hyperthermia Application, Nanomaterials and Energy, (2020) 1-7.
10. R.M. Borade, S.B. Somvanshi, S.B. Kale, R.P. Pawar, K.M. Jadhav, Spinel zinc ferrite nanoparticles: an active nanocatalyst for microwave irradiated solvent free synthesis of chalcones, Materials Research Express, (2020).
11. S.B. Kale, S.B. Somvanshi, M. Sarnaik, S. More, S. Shukla, K. Jadhav, Enhancement in surface area and magnetization of CoFe2O4 nanoparticles for targeted drug delivery application, in: AIP Conference Proceedings, AIP Publishing, 2018, pp. 030193.
12. S.B. Somvanshi, M.V. Khedkar, P.B. Kharat, K. Jadhav, Influential diamagnetic magnesium (Mg2+) ion substitution in nano-spinel zinc ferrite (ZnFe2O4): Thermal, structural, spectral, optical and physisorption analysis, Ceramics International, (2019).
13. S.B. Somvanshi, S.A. Jadhav, M.V. Khedkar, P.B. Kharat, S. More, K. Jadhav, Structural, thermal, spectral, optical and surface analysis of rare earth metal ion (Gd3+) doped mixed Zn–Mg nano-spinel ferrites, Ceramics International, (2020).
14. M. Babrekar, K. Jadhav, Synthesis and characterization of spray deposited lithium ferrite thin film, Int. Res. J. Sci. Eng. Special, (2017) 73-76.
15. G.L. Hornyak, CRC press, 2008.
16. S.W. Lee, Journal of Magnetism and Magnetic Materials, 310 (2007) 2868-2870.
17. D. Makovec, Journal of magnetism and magnetic materials, 289 (2005) 32-35.
18. S.B. Somvanshi, P.B. Kharat, M.V. Khedkar, K. Jadhav, Hydrophobic to hydrophilic surface transformation of nano-scale zinc ferrite via oleic acid coating: magnetic hyperthermia study towards biomedical applications, Ceramics International, 46 (2020) 7642-7653.
19. H. Kardile, S.B. Somvanshi, A.R. Chavan, A. Pandit, K. Jadhav, Effect of Cd2+ Doping on Structural, Morphological, Optical, Magnetic and Wettability Properties of Nickel Ferrite Thin Films, Optik, (2020) 164462.
20. P.B. Kharat, S.B. Somvanshi, K. Jadhav, Oleic Acid Coated Hydrophilic Nano-Scale Zinc Ferrite for Magnetic Hyperthermia Study towards Biomedical Applications, OUR SPONSORS, 45.
21. A. Bhosale, S.B. Somvanshi, V.D. Murumkar, K.M. Jadhav, Influential incorporation of RE metal ion (Dy3+) in yttrium iron garnet (YIG) nanoparticles: Magnetic, electrical and dielectric behaviour, Ceramics International, (2020).
22. M.V. Khedkar, S.B. Somvanshi, A.V. Humbe, K. Jadhav, Surface modified sodium silicate based superhydrophobic silica aerogels prepared via ambient pressure drying process, Journal of Non-Crystalline Solids, 511 (2019) 140-146.
23. D.N. Bhoyar, S.B. Somvanshi, P.B. Kharat, A. Pandit, K. Jadhav, Structural, infrared, magnetic and ferroelectric properties of Sr0· 5Ba0· 5Ti1-xFexO3 nanoceramics: Modifications via trivalent Fe ion doping, Physica B: Condensed Matter, 581 (2020) 411944.
24. J. Paulsen, Journal of Applied Physics, 97 (2005) 044502.
25. N. Sanpo, Acta Biomaterialia, 9 (2013) 5830-5837.
26. V. Kumbhar, Applied Surface Science, 259 (2012) 39-43.
27. P. Phong, Metallurgical and Materials Transactions A, 50 (2019) 1571-1581.
28. A.S. Priya, Vacuum, 160 (2019) 453-460.
29. K. Ugendar, Journal of Physics D: Applied Physics, 49 (2016) 305001.
30. J.S. Kounsalye, J. Mater. Sci. Mater. Electron., 28 (2017) 17254-17261.
31. A.V. Humbe, Ceram Int., (2017).
32. L. McCusker, J Appl Crystallogr., 32 (1999) 36-50.
33. P.N. Anantharamaiah, PCCP, 18 (2016) 10516-10527.
34. K.M. Batoo, J Alloys Compd., 726 (2017) 179-186.
35. K.B. Modi, Mater. Lett., 57 (2003) 4049-4053.
36. A.V. Humbe, J Alloys Comp., 691 (2017) 343-354.
37. R.D. Waldron, Physical Review, 99 (1955) 1727-1735.
38. S.C. Watawe, Int. J. Inorg. Mater., 3 (2001) 819-823.
39. B. Evans, J. Phy. & Chem. Solid, 29 (1968) 1573-1588.
40. K. Modi, J. Microw. Optoelectron., (2004) 223.
41. W. Wooster, Rep. Prog. Phys., 16 (1953) 62.
42. M.R. Patil, Int. J. Self-Propag. High-Temp Synth., 26 (2017) 33-39.